High-order magnetic resonance in the presence of strong longitudinal radio-frequency magnetic field based on atomic alignment states

Tao Shi, Ge Jin, and Sheng Zou ⬡*

Department of Instrument Science and Opto-Electronics Engineering, Beihang University, Beijing 100191, China;
Zhejiang Provincial Key Laboratory of Ultra-Weak Magnetic-Field Space and Applied Technology,
Hangzhou Innovation Institute of Beihang University, Hangzhou 310051, Zhejiang, China;
and Hefei National Laboratory, Hefei 230088, Anhui, China

A longitudinal radio-frequency (rf) magnetic field resonating at the Larmor frequency along the $\hat{z}$ direction in the presence of a static transverse magnetic field s investigated. Optical-radio-frequency double resonance in ^{85}Rb characterizes the strength of an external magnetic field through the precession frequency of ^{85}Rb atoms. The measurements are carried out in a paraffin-coated ^{85}Rb cell with a spin alignment configuration. An intriguing discovery of magnetic resonance peaks is observed at subharmonics of the Larmor frequency, accompanied by the emergence of nonlinear effects in the vicinity of the resonance. Notably, when the Larmor frequency reaches zero, the optical rotation signals induced by the rf magnetic field demonstrate a superposition of high-order harmonics of the rf frequency. Based on the simplified density matrix formalism and perturbation treatment, analytical expressions for the optical rotation are consistent with experimental outcomes. These findings hold the potential of extending our understanding on unveiling the dynamics of population and coherence among Zeeman sublevels, thereby advancing our knowledge in the field of alignment magnetometry.

I. INTRODUCTION

Since the pioneering work of Brossel and Bitter in the 1950s, the discovery of transitions between sublevels of the excited state induced by a radio-frequency field at the Larmor frequency, known as optical-radio-frequency double resonance, marked a pivotal moment in atomic physics [1]. This foundational work laid the groundwork for extensive investigations into energy levels, which have evolved into multifaceted fields contributing to various scientific pursuits. These pursuits included measuring population dynamics [2], exploring the coherence of Zeeman sublevels [3], and finding applications in advanced techniques recently such as atomic magnetometry [4,5], atomic clocks [6,7], and atom cooling [8].

In the presence of a low magnetic field (less than the geomagnetic field), transitions within each hyperfine manifold are degenerate. The transition frequencies remain independent of the hyperfine sublevels of the ground state but exhibit a linear dependence on the magnetic field, as described by the Breit-Rabi formula. The resulting frequency, referred to as the Larmor frequency, serves as a benchmark for comparison with the transverse driving field [9]. During the magnetic resonance process involving spin polarization induced by a circularly polarized laser [10], when the transverse driving field is significantly smaller than the bias field B_0, the rotating wave approximation [11] is often employed to solve the Bloch equation. Cohen-Tannoudji and colleagues [12] utilized Bessel functions to derive expressions for the magnetic resonance lineshape. When the amplitude of the driving field becomes comparable to or exceeds the bias field B_0, the effects of correction terms to the rotating wave approximation are revealed by making a Fourier expansion of the Bloch vector [13]. Sun and coworkers [14] observed subharmonics of the Larmor frequency in magnetic resonance curves and Bloch-Siegert shifts [15]. Their work employed Floquet perturbation theory [16] and numerical simulation of the Liouville equation [17] to elucidate these phenomena.

In the magnetic resonance process involving spin alignment created by a linearly polarized laser [18], if the transverse driving field is considerably smaller than the bias field B_0, the rotating wave approximation is applicable for solving the Liouville equation [19]. Sudyka and coworkers measured the Bloch-Siegert shifts and deformations of rf resonance curves in a low magnetic field. They also demonstrated the limitations of the rotating wave approximation. When the amplitude of the driving rf magnetic field was comparable to the bias field B_0, Zigdon and coworkers [20] observed magnetic resonance at the center of $\Omega_L/3$ and explained this experimental phenomenon using the Fourier expansion of the density matrix. Weis and coworkers [21] decomposed the density matrix of the Liouville equation in terms of atomic multipole moments and derived algebraic expressions for magnetic resonance lineshapes at the Larmor frequency under varying amplitudes of the driving rf magnetic field. Beato and coworkers [22] mapped two parametric resonances at zero field into the Hanle effect [23] and calculated analytical expressions for optical rotation signals using the dressed-atom approach.

*zousheng@buaa.edu.cn

In this paper, we utilize linearly polarized light to achieve n-rf photon resonance, exploring the distortion of a purely Lorentzian profile at the center of the Larmor frequency through the application of perturbation treatment. We extend this line of inquiry by investigating high-order magnetic resonance in the presence of a strong driving rf field. The orientation of the driving rf field B_{rf}, atomic alignment states A_0, and bias magnetic field B_0 all align along the $\hat{z}$ direction. When a small static magnetic field B_{x0} is applied along the $\hat{x}$ direction, resonance occurs, and magnetic resonance peaks emerge at subharmonics of the Larmor frequency (Ω_L/m, where m is an integer). Additionally, when the Larmor frequency is zero, optical rotation signals induced by the strong rf magnetic field exhibit a superposition of high-order harmonics of the rf frequency, described by the summation of high-order Bessel functions of the first kind. Simplifying the Liouville equation of the density matrix into two time-dependent equations, we derive analytical expressions for optical rotation based on these simplified equations and perturbation theory, thereby demonstrating consistency with experimental results. The organization of this paper is as follows. After describing the density-matrix formalism analysis in Sec. II, we present and discuss the experimental setup and results in Secs. III and IV, respectively, followed by the conclusion in Sec. V.

II. PRINCIPLES

The generation of spin states through the interaction of a polarized laser beam with an alkali atom is well established in physics. When the laser beam is circularly polarized, it propels the atom towards a polarized state, resulting in a nonzero average value of the $\hat{z}$ component of the spin polarization, particularly when the propagation of the pump light aligns with the $\hat{z}$ direction. However, a linearly polarized light induces a quadrupole or alignment of atoms along the polarization of the pumping light, forming a quadrupole with $3\langle\hat{s}_z\rangle^2 - \langle\hat{s}^2\rangle \neq 0$ when the propagation of the pump light aligns with the $\hat{z}$ direction. To accurately model the observed optical rotation signals of ^{85}Rb atoms interacting with linearly polarized probe and repump lights in a long relaxation time of a paraffin-coated cell, it is essential to consider both the probe and repump processes, as shown in Fig. 1. The central frequency of the linearly polarized probe laser is tuned on resonance of the $F_g = 3 \rightarrow F_e = 2$ hyperfine transition, and the intensity of the probe light is approximately $10\,\mu W$, corresponding to a Rabi frequency of $\Omega_{R_1} \approx 0.1\,\text{MHz}$. After several absorption and decay cycles, the $|m_F = \pm 3\rangle$ sublevels become equally populated, while the populations of the other sublevels decrease, resulting in alignment within the $F_g = 3$ states. However, a significant portion of atoms will be pumped out of the $F_g = 3 \rightarrow F_e = 2$ transition and populated into the hyperfine states in $F_g = 2$. To recover these lost atoms and form a closed $F_g = 3 \rightarrow F_e = 2$ transition, a repump laser is tuned on the resonance of the $F_g = 2 \rightarrow F_e = 2$ transition, which repumps the atoms in $F_g = 2$ back to $F_g = 3$ with a Rabi frequency of Ω_{R_2}, where $\Omega_{R_2} \gg \Omega_{R_1}$. The intensity of the repump light is about $200\,\mu W$, with a Rabi frequency of $\Omega_{R_2} \approx 2\,\text{MHz}$ much closer to the natural width of the excited state, with a value of $\Gamma = 5.75\,\text{MHz}$. This repump laser dramatically enhances the optical rotation signal without
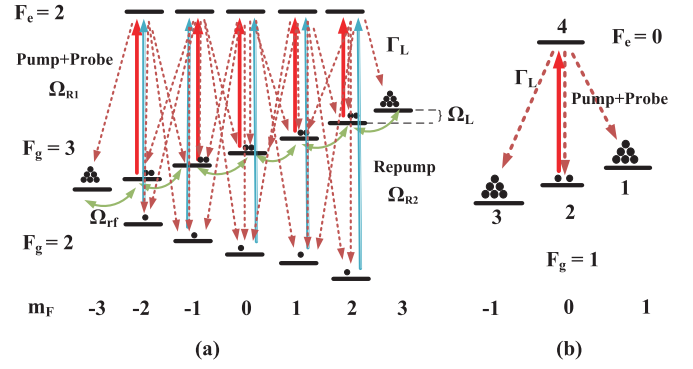

FIG. 1. The general diagram depicts the interaction of two linearly polarized lights with the $F_g = 2, 3 \rightarrow F_e = 2$ transitions. The probe light (red line) and the repump light (blue line) create alignment in the $F_g = 3$ states, with the quantization axis along the $\hat{z}$ direction. The ground Zeeman sublevels are separated by an energy equivalent to the Larmor frequency Ω_L. The magnetic Rabi frequency between these Zeeman sublevels is denoted as Ω_{rf} (green line). For clarity, we only depict the allowed spontaneous decay for the $|F_e = 2, m_F = 0\rangle$ state, as denoted by the red dashed line.

changing any atomic states in $F_g = 3$ Zeeman sublevels [24]. Since the atomic populations are mainly trapped in $|F_g = 3, m_F = \pm 3\rangle$ hyperfine states during the probe and repump processes, the system can be simplified into a scheme where one probe beam interacts with a four-level model containing $F_g = 1$ and $F_e = 0$ states, as mentioned in Ref. [20].

The atoms experience a $\hat{z}$-directed $\mathbf{B_0} = B_0\hat{z}$, corresponding to the Larmor frequency $\Omega_L = \mu_{eff}B_0$, where $\mu_{eff} = g\mu_B/(2I+1)$, μ_B represents the Bohr magneton, and g is the Landé factor (we set $\hbar = 1$), $g\mu_B = 2\pi \times 28\,\text{Hz/nT}$, nuclear spin $I = 5/2$. The alignment of the atoms is created and probed through the application of a linearly polarized beam, propagating in the $\hat{y}$ direction and having polarization in the $\hat{z}$ direction. Additionally, a driving rf magnetic field along the $\hat{z}$ direction, denoted as $\mathbf{B_{rf}} = B_1 \cos\omega t\hat{z}$, is introduced, giving rise to Rabi frequency $\omega_1 = \mu_{eff}B_1$. A transverse magnetic field $\sqrt{2}B_{x0}$ is in the $\hat{x}$ direction, corresponding to the frequency $\omega_{x0} = \mu_{eff}B_{x0}$. The Hamiltonian of this model is $H = \mu_{eff}\mathbf{F} \cdot \mathbf{B} + \mathbf{E} \cdot \mathbf{d_{eg}}$, where $\mathbf{d_{eg}}$ is the dipole operator [17]. In the Zeeman basis $|F_g = 1, m_F = 1\rangle = (1, 0, 0, 0)^T$, $|F_g = 1, m_F = 0\rangle = (0, 1, 0, 0)^T$, $|F_g = 1, m_F = -1\rangle = (0, 0, 1, 0)^T$, and $|F_e = 0, m_F = 0\rangle = (0, 0, 0, 1)^T$, the time-dependent Hamiltonian H under the rotating wave approximation is given by

$$H = \begin{pmatrix} \omega_z & \omega_{x0} & 0 & 0 \\ \omega_{x0} & 0 & \omega_{x0} & -\Omega_R \\ 0 & \omega_{x0} & -\omega_z & 0 \\ 0 & -\Omega_R & 0 & -\Delta \end{pmatrix}, \quad (1)$$

where the $\omega_z = \Omega_L + \omega_1 \cos\omega t$, Ω_R is the Rabi frequency of the optical transition induced by linearly polarized light, and $\Delta = \omega_l - \omega_0$ is the optical detuning [20]; ω_l is the frequency of the light and ω_0 is the frequency of $F_g = 3 \rightarrow F_e = 2$.

The time evolution of the density matrix ρ is governed by the Liouville equation [17], which is written in the form of

$$\frac{d\rho}{dt} = -i[H, \rho] - \frac{1}{2}\{\Gamma, \rho\} + \Lambda(\rho), \qquad (2)$$

where [,] denotes the commutator and { , } the anticommutator. The density matrix of the system is given by

$$\rho = \begin{pmatrix} \rho_{11} & \rho_{12} & \rho_{13} & \rho_{14} \\ \rho_{21} & \rho_{22} & \rho_{23} & \rho_{24} \\ \rho_{31} & \rho_{32} & \rho_{33} & \rho_{34} \\ \rho_{41} & \rho_{42} & \rho_{43} & \rho_{44} \end{pmatrix}. \qquad (3)$$

The relaxation of system is given by the matrix

$$\Gamma = \begin{pmatrix} \gamma_t & 0 & 0 & 0 \\ 0 & \gamma_t & 0 & 0 \\ 0 & 0 & \gamma_t & 0 \\ 0 & 0 & 0 & \gamma_t + \Gamma_L \end{pmatrix}, \qquad (4)$$

where the rate of spontaneous decay from the excited state is Γ_L, and both the ground and excited states undergo relaxation at a rate of γ_t as atoms exit the light beam. The matrix Λ is the repopulation of the ground state due to atoms entering the beam and spontaneous decay from the excited state [17], which is given by

$$\Lambda = \frac{1}{3}\begin{pmatrix} \gamma_t + \Gamma_L\rho_{44} & 0 & 0 & 0 \\ 0 & \gamma_t + \Gamma_L\rho_{44} & 0 & 0 \\ 0 & 0 & \gamma_t + \Gamma_L\rho_{44} & 0 \\ 0 & 0 & 0 & 0 \end{pmatrix}. \qquad (5)$$

The time derivatives of ρ_{14} and ρ_{34} that determine optical rotation signal ϕ can be written in the form of

$$\frac{d}{dt}\rho_{14} = -\left(\frac{\Gamma_L}{2} + \gamma_t - i\omega_z\right)\rho_{14} - i\Omega_R\rho_{12} - i\omega_{x0}\rho_{24},$$

$$\frac{d}{dt}\rho_{34} = -\left(\frac{\Gamma_L}{2} + \gamma_t + i\omega_z\right)\rho_{34} - i\Omega_R\rho_{32} - i\omega_{x0}\rho_{24}, \qquad (6)$$

given that $\Gamma_L \gg \omega_{x0}, \Omega_L, \omega_1, \gamma_t$, it is reasonable to assume that ρ_{12} and ρ_{32} are static over the integral time t and the value of ρ_{24} is negligible and can be omitted from Eq. (6), leading to a general solution in the form of

$$\rho_{14} \approx \frac{2i\Omega_R}{\Gamma_L}\rho_{12},$$

$$\rho_{34} \approx \frac{2i\Omega_R}{\Gamma_L}\rho_{32}, \qquad (7)$$

obviously, the optical rotation signal is determined by ρ_{12} and ρ_{32}. Using these relationship $\rho_{12} = -\rho_{23}$ and $\rho_{nm} = \rho_{mn}^*$, the in-phase and out-of-phase of observable optical-rotation signals after passing through the vapor cell are well defined in Ref. [20], which can be written in the form of

$$\phi^{\text{in}} = \frac{\lambda_0^2 n_0 \Gamma_L l}{8\sqrt{2}\pi \Omega_R}\text{Im}(\rho_{14} - \rho_{34}) = \frac{\lambda_0^2 n_0 l}{2\sqrt{2}\pi}\text{Re}\rho_{12},$$

$$\phi^{\text{out}} = \frac{\lambda_0^2 n_0 \Gamma_L l}{8\sqrt{2}\pi \Omega_R}\text{Re}(\rho_{14} + \rho_{34}) = \frac{\lambda_0^2 n_0 l}{2\sqrt{2}\pi}\text{Im}\rho_{12}, \qquad (8)$$

where λ_0 refers to the wavelength of probe beam, n_0 is the alkali vapor density, and l is the optical length. In the case of

weak probe light and transverse magnetic field, we notice that the magnetic field does not significantly alter the population from the steady states. Using this assumption and above equation (7), the time evolution of 16 elements are contracted into two equations, ρ_{12} and ρ_{13}, which are briefly expressed in the form of

$$\begin{pmatrix} \dot{\rho}_{12} \\ \dot{\rho}_{13} \end{pmatrix} = \mathcal{M}\begin{pmatrix} \rho_{12} \\ \rho_{13} \end{pmatrix} + \begin{pmatrix} i\omega_{x0}A_0 \\ 0 \end{pmatrix}, \qquad (9)$$

where the matrix $\mathcal{M}$ is

$$\mathcal{M} = \begin{pmatrix} -R_{\text{rel}} - i\omega_z & i\omega_{x0} \\ 2i\omega_{x0} & -\gamma_t - 2i\omega_z \end{pmatrix}, \qquad (10)$$

defining $\kappa = 2\Omega_R^2/\Gamma_L$ as the relaxation rate caused by probe light, the total relaxation rate R_{rel} is $\gamma_t + \kappa$. The steady-state solutions of the population are $\rho_{11}^s = (\gamma_t + 2\kappa)/(3\gamma_t + 4\kappa)$ and $\rho_{22}^s = \gamma_t/(3\gamma_t + 4\kappa)$. The equilibrium alignment A_0 is $\rho_{11}^s - \rho_{22}^s = 2\kappa/(3\gamma_t + 4\kappa)$. A_0 is similar to polarization P_0 in the Bloch equation of Ref. [25], which describes the alignment state of atoms created by polarized light. In general, this Eq. (9) can be solved analytically by perturbation technique [26]. We replace ω_{x0} in Eq. (9) by $\lambda\omega_{x0}$, where λ is a parameter ranging between zero and one that characterizes the strength of the perturbation. We now search for a solution to Eq. (9), expressed as a power series with respect to λ is given as

$$\rho_{mn} = \rho_{mn}^{(0)} + \lambda\rho_{mn}^{(1)} + \lambda^2\rho_{mn}^{(2)} + \cdots, \qquad (11)$$

we require that Eq. (11) be a solution of Eq. (9) for any value of the parameter λ. To hold this condition, each coefficient of power series with respect to λ should satisfy Eq. (9) separately. It is not difficult to find $\rho_{12}^{(2n)} = 0$, $\rho_{23}^{(2n)} = 0$, $\rho_{13}^{(0)} = 0$, and $\rho_{13}^{(2n-1)} = 0$, where n is the integer. We thereby obtain the first-order derivative $\dot{\rho}_{12}^{(1)}$ as

$$\dot{\rho}_{12}^{(1)} = -[\gamma_t + \kappa + i(\Omega_L + \omega_1\cos\omega t)]\rho_{12}^{(1)} + i\omega_{x0}A_0. \qquad (12)$$

To simplify the integral calculation, we choose a set of initial states $\rho_{11}^{(0)} = \rho_{11}^s$, $\rho_{22}^{(0)} = \rho_{22}^s$, $\rho_{12}^{(1)}(0) = 0$, $\rho_{32}^{(1)}(0) = 0$, $\rho_{12} = -\rho_{23}$, $\rho_{23} = \rho_{32}^*$. When employing these initial states into Eq. (12), the solution can be written as

$$\rho_{12}^{(1)} = i\omega_{x0}A_0\sum_{m=-\infty}^{m=+\infty}\sum_{n=-\infty}^{n=+\infty}\frac{J_m(\beta)J_n(\beta)e^{i(m-n)\omega t}}{R_{\text{rel}} + i(\Omega_L + m\omega)}, \qquad (13)$$

where $\beta = \omega_1/\omega$ is the modulation parameter and $J_m(\beta)$ is the first kind of Bessel function. For a large modulation parameter, such as $\beta = 1$, the high-order derivatives of $\dot{\rho}_{13}^{(2)}$ and $\dot{\rho}_{12}^{(3)}$ should be taken into consideration. The solutions of $\dot{\rho}_{13}^{(2)}$ and $\dot{\rho}_{12}^{(3)}$ are given in the Appendix.

III. EXPERIMENTAL SETUP

Figure 2 depicts a schematic of the experimental setup employed in this study. The experiment utilizes a spherical cell with a diameter of 5 cm, containing a natural abundance rubidium. The antirelaxation coating on the cell enhances the coherence time between ground Zeeman sublevels, as evidenced by the measured half maximum and half width of the magnetic resonance curve in Fig. 4(d), which is $\Delta v = 5$ Hz. The cell is maintained at room temperature and is positioned
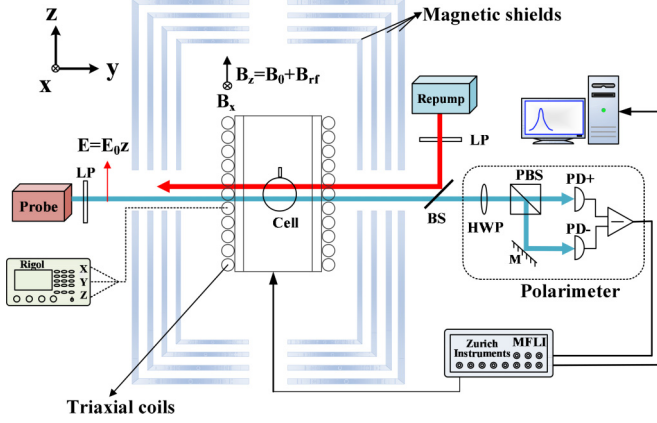
FIG. 2. Schematic of the experimental setup. A triaxial coil constructed by Lee-Whiting coils and saddle coils, is designed to provide a static or oscillated magnetic field. The static magnetic field direction is along the $\hat{z}$ direction, which generated by a signal generator. A driving rf field along the $\hat{z}$ direction is produced by a signal generator. The repump and probe beams, emitted from a distributed feedback laser and separated by about 5 mm, propagate along the $\hat{y}$ direction with the initial polarization along the $\hat{z}$ direction. Optical rotation signal of probe beam induced by atoms is detected and analyzed by a polarimeter and lock-in amplifier. A polarimeter contains a pair of photodiodes PD+ and PD−, a mirror, HWP, and PBS. LP is linearly polarized plate; HWP is half-wave plate; PD is photodiode; PBS is polarized beam splitter.

within a four-layer cylindrical μ-metal shielding for magnetic field with a shielding factor of approximately 10^4.

A triaxial coil, designed using Lee-Whiting coils and saddle coils, is employed to provide either a static or oscillating magnetic field [27]. The large static magnetic field is directed
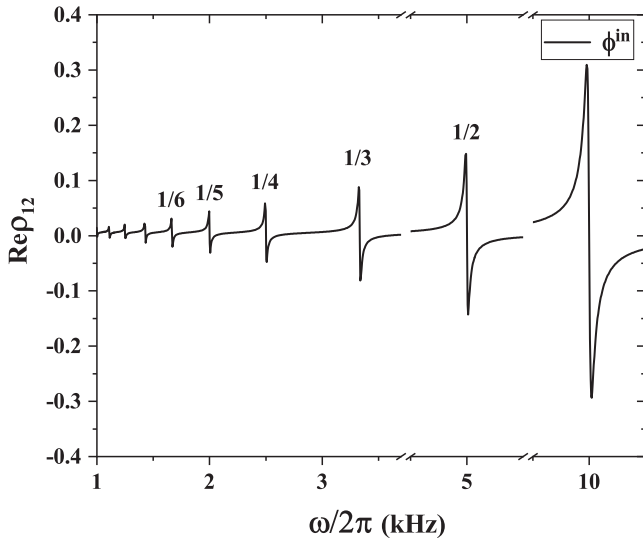

FIG. 3. The distributions of the magnetic resonance curves are centered at Ω_L/m, where m can be numerically simulated by Eq. (9). The transverse frequency $\omega_{x0} = 2\pi \times 5$ Hz, $A_0 = 0.2$, the Larmor frequency $\Omega_L = 2\pi \times 10$ kHz. The rf field with amplitude of $\omega_1 = 0.8\Omega_L$ and frequency of ω varying from $2\pi \times 90$ Hz to $2\pi \times 10.1$ kHz.
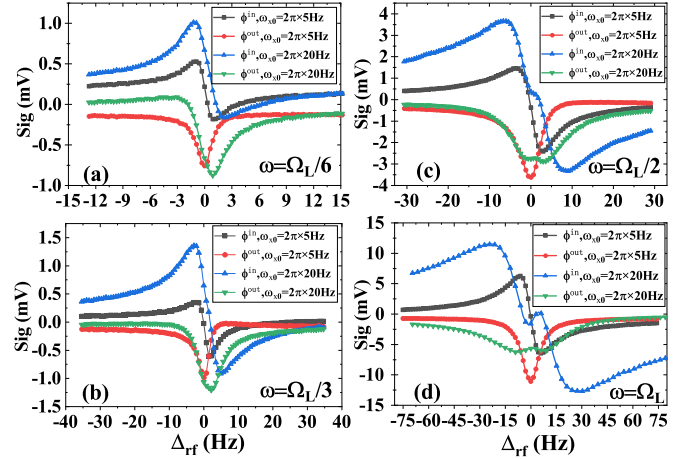

FIG. 4. Magnetic resonance peaks were observed at subharmonics of the Larmor frequency with the same gain of photodiode amplifier under two different transverse frequencies $\omega_{x0} = 2\pi \times 5$ Hz and $2\pi \times 20$ Hz. (a)–(d) are magnetic resonance curves centered at frequency of $\Omega_L/6$, $\Omega_L/3$, $\Omega_L/2$, and Ω_L. The nonlinear effect near the resonance frequency shown in blue triangle lines and green inverted triangle lines in (c) and (d) can be interpreted by Eqs. (13) and (A2b).

along the $\hat{z}$ direction and generated by a signal generator. We align the quantization axis along the $\hat{z}$ direction. The driving rf magnetic field along the $\hat{z}$ direction is produced by the sine wave output of a signal generator.

Two beams, emitted from a distributed feedback laser and separated by approximately 5 mm, propagate along the $\hat{y}$ direction with the initial polarization along the $\hat{z}$ direction, serving as the repump and probe beams. The repump light is tuned on the resonance of the $F_g = 2 \rightarrow F_e = 2$ transition, while the probe light is tuned on the resonance of the $F_g = 3 \rightarrow F_e = 2$ transition to maximize the optical rotation signal. The intensity of the probe light is 10 μW with a $1/e^2$ beam diameter of approximately 5 mm. The intensity of the repump light is 200 μW with a $1/e^2$ beam diameter of about 5 mm. After passing through the vapor cell, the polarization of the probe beam is analyzed using a balanced polarimeter, consisting of a polarizing beam splitter and two photodiodes detecting the intensities of the two beams. The output signal is extracted by a lock-in amplifier.

IV. RESULTS AND DISCUSSION

A. High-order magnetic resonances at subharmonics of the Larmor frequency

In the absence of transverse magnetic field, there is no resonance occurring. When a small transverse static magnetic field $B_{x0} = 1.07$ nT is applied, corresponding to transverse frequency $\omega_{x0} = 5$ Hz $(\leqslant R_{\text{rel}})$, Eq. (13) predicts that the high-order magnetic resonances appeared at center of $\omega = \Omega_L/m$ after being demodulated at frequency of ω. Numeric simulations of Eq. (9) demodulated at first harmonic of ω are depicted in Fig. 3. The parameters used in the calculation are $R_{\text{rel}} = 2\pi \times 10$ Hz, $\beta = 2\pi \times 800$ Hz$/\omega$, $\Omega_L = 2\pi \times 10$ kHz, $\omega_{x0} = 2\pi \times 5$ Hz, and $A_0 = 0.2$. In the

experiment, the intensity of probe light is $10\,\mu\text{W}$, the transverse magnetic field $B_{x0} = 1.07\,\text{nT}$, the bias magnetic field $B_0 = 2.14\,\mu\text{T}$, the rf field with amplitude of $B_1 = 0.8B_0$, and the sweeping frequency of ω starting from $0.01\Omega_L$ to $1.1\Omega_L$ is along the $\hat{z}$ direction. After demodulating at a frequency of ω, the profiles of the magnetic resonance curves follow a Lorentzian distribution. The center frequency is Ω_L/m, where m is an integer. We choose $m = 1, 2, 3, 6$ and plot them in Fig. 4. The half maximum and full width of Lorentzian curve resonated at $\Omega_L = 2\pi \times 10\,\text{kHz}$ is approximately 10 Hz as depicted in Fig. 4(d). At the center of $\Omega_L/6$, magnetic resonance curves are shown in Fig. 4(a), the half maximum and full width of the black square line is about six times narrower than the Lorentzian curve resonating at Ω_L.

If the transverse magnetic field $B_{x0} = 4.28\,\text{nT}$, ω_{x0} is comparable to the relaxation rate, for example, $\omega_{x0} = 2\pi \times 20\,\text{Hz}$, then higher orders of λ come into play. The nonlinear effects, as shown in Refs. [20,21], also occur at the center of Ω_L and $\Omega_L/2$, as depicted by the blue triangle lines and green inverted triangle lines in Figs. 4(c) and 4(d). Continuing to increase the value of ω_{x0} up to Ω_L and nullifying the static magnetic field along the $\hat{z}$ axis, this scheme is similar to that mentioned in Ref. [20], where resonance peaks only appear at the center of $\Omega_L/(2m - 1)$, where m is a positive integer. The equation that expressed magnetic resonance at the center of Ω_L can be carried out by substituting $m = -1$, $m - n + q = -2$, $m - n + q - p + k = -1$, and $m - n + q - p + k - l = -1$ into Eqs. (13) and (A2b), which are simplified into

$$\rho_{12}^{m} = \rho_{12}^{ms} + \rho_{12}^{mt}, \tag{14}$$

where

$$\rho_{12}^{ms} = -i\omega_{x0}A_0 \frac{J_0(\beta)J_1(\beta)}{R_{rel} + i(\Omega_L - \omega)}, \tag{15}$$

and

$$\rho_{12}^{mt} = -\rho_{12}^{ms}2\omega_{x0}^2 \sum_{p=-\infty}^{p=+\infty}\sum_{q=-\infty}^{q=+\infty}\left(\frac{J_{p+1}(\beta)J_{q+1}(\beta)}{R_{rel} + i(\Omega_L - \omega)}\right.$$
$$\left.\times\frac{J_p(2\beta)J_q(2\beta)}{\gamma_t + 2i(\Omega_L - \omega)}\right), \tag{16}$$

ρ_{12}^{ms} is a steady-state part and ρ_{12}^{mt} is a time-dependent part. ρ_{12}^{ms} is the term that Eq. (13) resonance at frequency of Ω_L. Substituting Eq. (14) into Eq. (8), the in-phase and quadrature optical rotation signals are

$$\phi_f^{in} = \frac{\lambda_0^2 n_0 l}{2\sqrt{2\pi}}\text{Re}\rho_{12}^{m}, \tag{17a}$$

$$\phi_f^{out} = \frac{\lambda_0^2 n_0 l}{2\sqrt{2\pi}}\text{Im}\rho_{12}^{m}. \tag{17b}$$

To simulate Eq. (14), we set $\gamma_t = 2\pi \times 10\,\text{Hz}$, $\omega_{x0} = 2\pi \times 20\,\text{Hz}$, $\kappa = 2\pi \times 10\,\text{Hz}$, $\omega_1 = 2\pi \times 10\,\text{kHz}$, $\Omega_L = 2\pi \times 10\,\text{kHz}$, and ω varying from 9.85 kHz to 10.15 kHz, indices of summations p and q range from -6 to 6, these values all correspond to the experimental parameters. The simulation results are plotted in Fig. 5, two black square lines are the real and imaginary parts of Eq. (14), the two red dotted lines are the real and imaginary parts of Eq. (15), and the two triangular lines are the real and imaginary parts of Eq. (16).
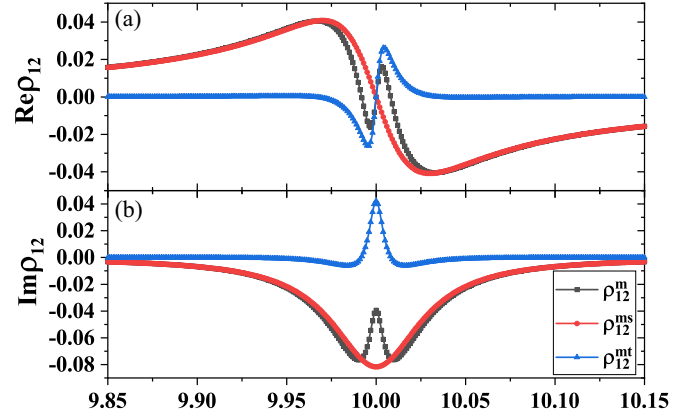

FIG. 5. Magnetic resonance curves at center of $\Omega_L = 2\pi \times 10\,\text{kHz}$ simulated by perturbation theory. (a) shows the real part of ρ_{12}^{ms}, ρ_{12}^{mt}, and ρ_{12}^{m}. (b) is imaginary part of ρ_{12}^{ms}, ρ_{12}^{mt}, and ρ_{12}^{m}. The deformations of Lorentzian magnetic resonance curves come from $\rho_{12}^{(3)}$.

We found the nonlinear effect near the resonance coming from the derived term of the third-order λ. However, when the ω_{x0} is larger than the relaxation rate γ_t, perturbation theory is not valid, thus, we need go back to Eq. (9) and utilize the fourth-order Runge-Kutta method to numerically simulate the fraction of magnetic resonance curves.

B. Zero field and large modulation parameters

When Ω_L is close to zero, for $R_{rel} \geqslant \omega$, we use the dc component of Eq. (A2b) to calculate the integration of Eq. (A1b), which can be written in the form of

$$\rho_{12}^{h} = iA_0'e^{-i\beta\sin\omega t}\sum_{m=-\infty}^{m=+\infty}\frac{J_m(\beta)e^{im\omega t}}{R_{rel} + im\omega}, \tag{18}$$

where

$$A_0' = \omega_{x0}A_0\left(1 - \frac{2\omega_{x0}^2 J_0(\beta)^2 J_0(2\beta)^2}{R_{rel}\gamma_t}\right).$$

Substituting Eq. (18) into Eq. (8), the general form of the optical rotation signal available in the regime of high rf power could be given by

$$\phi_h = G_0 \frac{\lambda_0^2 n_0 l}{2\sqrt{2\pi}}\text{Re}\rho_{12}^{h}, \tag{19}$$

where the l is optical length and G_0 is a scaling factor to ensure alignment with the signal's amplitude.

In the case of low rf power, characterized by a small modulation parameter β, for example, $\beta = 0.05$, only the $m = 0$ and $m = \pm 1$ terms in Eq. (19) are significant. By employing the Jacobi-Anger expansion Eq. (A3) into Eq. (18) to expand the $e^{i\beta\sin\omega t}$, and omitting the dc component while retaining the low order of Bessel functions, the optical rotation signals in this regime can be simplified into

$$\phi_s = G_0 \frac{A_0'\lambda_0^2 n_0 l}{\sqrt{2\pi}R_{rel}}J_0(\beta)J_1(\beta)\sin\omega t, \tag{20}$$

the static magnetic field in the $\hat{x}$, $\hat{y}$, and $\hat{z}$ axes are 21.4 pT, zero, and zero, respectively. The spin relaxation rate R_{rel} is
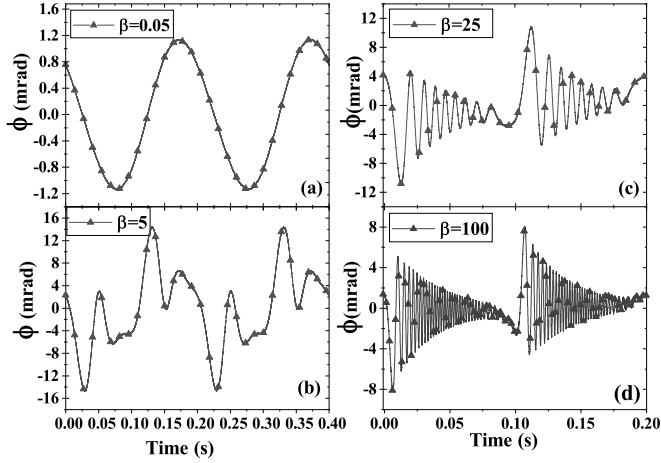
FIG. 6. Measurements of optical rotation signal at different modulation parameters of β. The static magnetic field in $\hat{x}$ direction is about 21.4 pT, which in $\hat{y}$ and $\hat{z}$ axes are zero. The relaxation rate $R_{\rm rel} = 2\pi \times 10$ Hz. The triangles are experimental data and black lines are numerical fitting curves.

$2\pi \times 10$ Hz. The intensity of the probe light is $10\,\mu$W. Figure 6 shows the optical rotation signals at different modulation parameters of β. The black triangles in Fig. 6(a) show the $\beta = 0.05$ which is explained by Eq. (19). When the power of the rf field is increased, the high order of Bessel function in Eq. (19) should be taken into consideration. The curves depicted in Figs. 6(b), 6(c) and 6(d) are the superpositions of different harmonic waves.

We substitute parameters $\gamma_t = 2\pi \times 1$ Hz, $\omega_{x0} = 2\pi \times 0.1$ Hz, $\kappa = 2\pi \times 3$ Hz, $\omega = 2\pi \times 5$ Hz, $\lambda_0 = 794.9825$ nm, the saturated vapor density $n_0 = 1.27 \times 10^{10}/{\rm cm}^3$, $l = 5$ cm, $G_0 \approx 0.07$ into Eqs. (9) and (19), and we plot the optical rotation angle ϕ_h at different modulation parameters, $\beta = 0.05, 5, 25, 100$ as shown in Fig. 6. Moreover, we could also use these parameters to calculate the numeric solution of Eq. (9). The theoretical solutions obtained by perturbation theory and numerical simulation based on the simplified Eq. (9) are both consistent with the experimental data.

V. CONCLUSION

In summary, our investigation into high-order magnetic resonances of spin alignment in the presence of a longitudinal rf field, both theoretically and experimentally, has yielded insightful results. Specifically, when a longitudinal driving rf magnetic field resonates at the Larmor frequency along the $\hat{z}$

direction, in the presence of a small static magnetic field in the transverse plane, we observed magnetic resonance peaks at the center of fractional Larmor frequencies, accompanied by the emergence of nonlinear effects near the resonance frequency.

Furthermore, our study revealed that when the Larmor frequency reached zero, optical rotation signals induced by a rf magnetic field exhibit a superposition of high-order harmonics of the rf frequency. This phenomenon is accurately described by the summation of high-order Bessel functions of the first kind. A key highlight of our work lies in the simplification of the time-derivative equations governing the 16 density matrix elements into two equations, primarily concerning ρ_{12} and ρ_{13}, which predominantly determine the optical rotation angle. These simplified equations can be easily solved using Jacobi-Anger expansion and perturbation theory. Importantly, the analytical expressions derived for optical rotation signals align well with our experimental results.

These findings hold promise for extending our understanding of the dynamics of alignment states. The ability to accurately model and manipulate high-order magnetic resonances opens avenues for advancing both theoretical and practical aspects of spin alignment, with implications for improving the performance of magnetometers.

APPENDIX: CALCULATION OF HIGH ORDER λ OF ρ_{12} AND ρ_{13} BY PERTURBATION METHOD

Starting from Eq. (13), the general solution of $\dot{\rho}_{13}^{(2)}$ and $\dot{\rho}_{12}^{(3)}$ are in the form of

$$
\rho_{13}^{(2)} = 2i\omega_{x0} e^{-(\gamma_t + 2i\Omega_L)t + 2i\beta \sin \omega t}
$$
$$
\times \int_0^t e^{(\gamma_t + 2i\Omega_L)t_1 + 2i\beta \sin \omega t_1} \rho_{12}^{(1)} dt_1, \quad \text{(A1a)}
$$

$$
\rho_{12}^{(3)} = i\omega_{x0} e^{-(R_{\rm rel} + i\Omega_L)t + i\beta \sin \omega t}
$$
$$
\times \int_0^t e^{(R_{\rm rel} + i\Omega_L)t_1 + i\beta \sin \omega t_1} \rho_{13}^{(2)} dt_1, \quad \text{(A1b)}
$$

Equation (A1) can be expanded by Jacobi-Anger expressions and then take the integration, which can be shown as

$$
\rho_{13}^{(2)} = -2\omega_{x0}^2 A_0 \sum_{p=-\infty}^{p=+\infty} \sum_{q=-\infty}^{q=+\infty} \sum_{m=-\infty}^{m=+\infty} \sum_{n=-\infty}^{n=+\infty} \left(\frac{J_m(\beta)J_n(\beta)e^{i(m-n)\omega t}}{R_{\rm rel} + i(\Omega_L + m\omega)} \frac{J_p(2\beta)J_q(2\beta)e^{i(q-p)\omega t}}{\gamma_t + i(\Omega_L + (m-n+q)\omega)} \right), \quad \text{(A2a)}
$$

$$
\rho_{12}^{(3)} = -2i\omega_{x0}^3 A_0 \sum_{l=-\infty}^{l=+\infty} \sum_{k=-\infty}^{k=+\infty} \sum_{p=-\infty}^{p=+\infty} \sum_{q=-\infty}^{q=+\infty} \sum_{m=-\infty}^{m=+\infty} \sum_{n=-\infty}^{n=+\infty} \left(\frac{J_m(\beta)J_n(\beta)e^{i(m-n)\omega t}}{R_{\rm rel} + i(\Omega_L + m\omega)} \right.
$$
$$
\left. \times \frac{J_p(2\beta)J_q(2\beta)e^{i(q-p)\omega t}}{\gamma_t + i(2\Omega_L + (m-n+q)\omega)} \frac{J_k(\beta)e^{i(k-l)\omega t}}{R_{\rm rel} + i(\Omega_L + (m-n+q-p+k)\omega)} \right), \quad \text{(A2b)}
$$

where the Jacobi-Anger expansion [28] is

$$e^{i\beta \sin \omega t} = \sum_{m=-\infty}^{+\infty} J_m(\beta) e^{i\omega t}. \tag{A3}$$

[1] J. Brossel and F. Bitter, A new "double resonance" method for investigating atomic energy levels. Application to Hg $^3 p_1$, Phys. Rev. **86**, 308 (1952).

[2] T. Krehlik, A. Stabrawa, R. Gartman, K. T. Kaczmarek, R. Löw, and A. Wojciechowski, Zeeman optical pumping of ^{87}Rb atoms in a hollow-core photonic crystal fiber, Opt. Lett. **47**, 5731 (2022).

[3] F. Sarreshtedari, A. Rashedi, F. Ghashghaei, and M. Sabooni, Engineering of the Cesium Zeeman sublevel populations using sequences of laser pulses and RF excitation, Phys. Scr. **96**, 015401 (2021).

[4] S. Zou, H. Zhang, X. Chen, and J. Fang, In-situ triaxial residual magnetic field measurement based on optically-detected electron paramagnetic resonance of spin-polarized potassium, Measurement **187**, 110338 (2022).

[5] R. Li, Y. Liu, L. Cao, S. Li, J. Li, and Y. Zhai, Parameter optimisation of miniaturised SERF magnetometer below relaxation rate saturation region, Measurement **214**, 112733 (2023).

[6] H. Cheng, S. Deng, Z. Zhang, J. Xiang, J. Ji, W. Ren, T. Li, Q. Qu, L. Liu, and D. Lü, Uncertainty evaluation of the second-order Zeeman shift of a transportable ^{87}Rb atomic fountain clock, Chinese Optics Letters **19**, 120201 (2021).

[7] J.-Y. Liou, C.-E. Wu, H.-J. Su, and Y.-H. Chen, Optimizing population accumulation in a designated single Zeeman state using microwave spectroscopy, Optics Continuum **2**, 2017 (2023).

[8] M. Frometa, J. Lopez, and J. Tabosa, Magnetically assisted optical gain in Zeeman degenerate two-level systems of cold atoms, Opt. Commun. **433**, 111 (2019).

[9] G. Breit and I. Rabi, Measurement of nuclear spin, Phys. Rev. **38**, 2082 (1931).

[10] W. Happer, Optical pumping, Rev. Mod. Phys. **44**, 169 (1972).

[11] I. I. Rabi, N. Ramsey, and J. Schwinger, Use of rotating coordinates in magnetic resonance problems, Rev. Mod. Phys. **26**, 167 (1954).

[12] C. Cohen-Tannoudji, J. Dupont-Roc, S. Haroche, and F. Laloë, Diverses résonances de croisement de niveaux sur des atomes pompés optiquement en champ nul. i. théorie, Revue de physique appliquée **5**, 95 (1970).

[13] S. Stenholm, Saturation effects in RF spectroscopy. I. General theory, J. Phys. B **5**, 878 (1972).

[14] Y. Sun, Y. Xu, and Z. Wang, The multi-RF photon transition driven by strong RF field in optical magnetic resonance of atoms, Opt. Laser Technol. **145**, 107488 (2022).

[15] F. Bloch and A. Siegert, Magnetic resonance for nonrotating fields, Phys. Rev. **57**, 522 (1940).

[16] M. Leskes, P. Madhu, and S. Vega, Floquet theory in solid-state nuclear magnetic resonance, Prog. Nucl. Magn. Reson. Spectrosc. **57**, 345 (2010).

[17] M. Auzinsh, D. Budker, and S. Rochester, *Optically Polarized Atoms: Understanding Light-Atom Interactions* (Oxford University Press, New York, 2010).

[18] D. Budker, D. F. Kimball, V. V. Yashchuk, and M. Zolotorev, Nonlinear magneto-optical rotation with frequency-modulated light, Phys. Rev. A **65**, 055403 (2002).

[19] J. Sudyka, S. Pustelny, and W. Gawlik, Limitations of rotating-wave approximation in magnetic resonance: characterization and elimination of the Bloch–Siegert shift in magneto-optics, New J. Phys. **21**, 023024 (2019).

[20] T. Zigdon, A. Wilson-Gordon, S. Guttikonda, E. Bahr, O. Neitzke, S. Rochester, and D. Budker, Nonlinear magneto-optical rotation in the presence of a radio-frequency field, Opt. Express **18**, 25494 (2010).

[21] A. Weis, G. Bison, and A. S. Pazgalev, Theory of double resonance magnetometers based on atomic alignment, Phys. Rev. A **74**, 033401 (2006).

[22] F. Beato, E. Belorizky, E. Labyt, M. Le Prado, and A. Palacios-Laloy, Theory of a ^{4}He parametric-resonance magnetometer based on atomic alignment, Phys. Rev. A **98**, 053431 (2018).

[23] E. Breschi and A. Weis, Ground-state Hanle effect based on atomic alignment, Phys. Rev. A **86**, 053427 (2012).

[24] R. Li, C. Perrella, and A. Luiten, Repumping atomic media for an enhanced sensitivity atomic magnetometer, Opt. Express **30**, 31752 (2022).

[25] M. P. Ledbetter, I. M. Savukov, V. M. Acosta, D. Budker, and M. V. Romalis, Spin-exchange-relaxation-free magnetometry with CS vapor, Phys. Rev. A **77**, 033408 (2008).

[26] R. Zhang, Z.-G. Wang, X. Peng, W.-H. Li, S.-J. Li, and H. Guo, Spin dynamics of magnetic resonance with parametric modulation in a potassium vapor cell, Chin. Phys. B **26**, 030701 (2017).

[27] H. Pang, W. Fan, F. Liu, Z. Wu, Q. Yuan, P. Du, X. Zhou, and W. Quan, Analysis and improvement of the uniformity of magnetic field coil based on the cylindrical magnetic shield in atomic magnetometers, Sensors and Actuators A: Physical **349**, 114005 (2023).

[28] M. Abramowitz and I. A. Stegun, *Handbook of Mathematical Functions with Formulas, Graphs, and Mathematical Tables* (US Government printing office, Washington DC, 1968), Vol. 55.